Analytica Chimica Acta 1287 (2024) 342091

Contents lists available at ScienceDirect

Analytica Chimica Acta

journal homepage: www.elsevier.com/locate/aca

Ternary electrochemiluminescence quenching effects of $CuFe_2O_4$@PDA-MB towards self-enhanced $Ru(dcbpy)_3^{2+}$ functionalized 2D metal-organic layer and application in carcinoembryonic antigen immunosensing

Xiang Ren [a,b,*], Zuoxun Xie [b], Huan Wang [b], Lijun Wang [c], Zhongfeng Gao [b], Hongmin Ma [b], Nuo Zhang [b], Dawei Fan [b], Qin Wei [b,**], Huangxian Ju [a,***]

[a] State Key Laboratory of Analytical Chemistry for Life Science, School of Chemistry and Chemical Engineering, Nanjing University, Nanjing, 210023, PR China
[b] Key Laboratory of Chemical Sensing & Analysis in Universities of Shandong, Collaborative Innovation Center for Green Chemical Manufacturing and Accurate Detection, School of Chemistry and Chemical Engineering, University of Jinan, Jinan, 250022, PR China
[c] Shandong Institute of Mechanical Design and Research, School of Mechanical Engineering, QiLu University of Technology (Shandong Academy of Sciences), PR China

HIGHLIGHTS

- ECL signal originated from intramolecular co-reaction between PEI and $Ru(dcbpy)_3^{2+}$.
- $CuFe_2O_4$@PDA-MB quenches the excited states of $Ru(dcbpy)_3^{2+}$ by PDA, Cu^{2+}, and MB.
- ECL signal quenching of $Ru(dcbpy)_3^{2+}$ by MB was explained by the inner filter effect.
- High-performance ECL immunosensing of CEA.

GRAPHICAL ABSTRACT

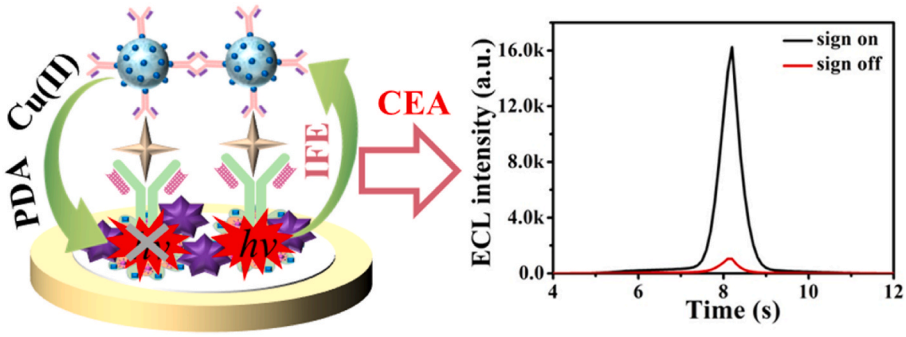

ARTICLE INFO

Handling editor: Nicola Cioffi

Keywords:
Electrochemiluminescence sensor
Carcinoembryonic antigen
$Ru(dcbpy)_3^{2+}$
Quenching probe
Self-enhanced

ABSTRACT

Background: Carcinoembryonic antigen (CEA) is a significant glycosylated protein, and the unusual expression of CEA in human serum is used as a tumor marker in the clinical diagnosis of many cancers. Although scientists have reported many ways to detect CEA in recent years, such as electrochemistry, photoelectrochemistry, and fluorescence, their operation is complex and sensitivity is average. Therefore, finding a convenient method to accurately detect CEA is significance for the prevention of malignant tumors. With high sensitivity, quick reaction, and low background, electrochemiluminescence (ECL) has emerged as an essential method for the detection of tumor markers in blood.

Results: In this work, a "signal on-off" ECL immunosensor for sensitive analysis of CEA ground on the ternary extinction effects of $CuFe_2O_4$@PDA-MB towards a self-enhanced $Ru(dcbpy)_3^{2+}$ functionalized metal-organic layer

* Corresponding author. State Key Laboratory of Analytical Chemistry for Life Science, School of Chemistry and Chemical Engineering, Nanjing University, Nanjing, 210023, PR China.
** Corresponding author.
*** Corresponding author.
E-mail addresses: chem_renx@163.com (X. Ren), sdjndxwq@163.com (Q. Wei), hxju@nju.edu.cn (H. Ju).

https://doi.org/10.1016/j.aca.2023.342091
Received 6 September 2023; Received in revised form 8 November 2023; Accepted 29 November 2023
Available online 2 December 2023

[(Hf)MOL-Ru-PEI-Pd] was prepared. The high ECL efficiency of (Hf)MOL-Ru-PEI-Pd originated from the dual intramolecular self-catalysis, including intramolecular co-reaction between polyethylenimine (PEI) and Ru(dcbpy)$_3^{2+}$. At the same time, loading Pd NPs onto (Hf)MOL-Ru-PEI could not only improve the electron transfer ability of (Hf)MOL-Ru-PEI, but also provide more active sites for the reaction of Ru(dcbpy)$_3^{2+}$ and PEI. In the presence of CEA, $CuFe_2O_4$@PDA-MB-Ab$_2$ efficiently quenches the excited states of (Hf)MOL-Ru-PEI-Pd by PDA, Cu^{2+}, and methylene blue (MB) via energy and electron transfer, leading to an ECL signal decrease. Under optimal conditions, the proposed CEA sensing strategy showed satisfactory properties ranging from 0.1 pg mL^{-1} to 100 ng mL^{-1} with a detection limit of 20 fg mL^{-1}.

Significance: The (Hf)MOL-Ru-PEI-Pd and $CuFe_2O_4$@PDA-MB were prepared in this work might open up innovative directions to synthesize luminescence-functionalized MOLs and effective quencher. Besides, the ECL quenching mechanism of Ru(dcbpy)$_3^{2+}$ by MB was successfully explained by the inner filter effect (ECL-IFE). At last, the proposed immunosensor exhibits excellent repeatability, stability, and selectivity, and may provide an attractive way for CEA and other disease markers determination.

1. Introduction

Carcinoembryonic antigen (CEA) is a significant glycosylated protein, and the unusual expression of CEA in human serum is used as a tumor marker in the clinical diagnosis of pancreatic, colorectal, and gastric cancer [1]. Although scientists have reported many ways to detect CEA in recent years, such as electrochemistry [2], photoelectrochemistry [3], and fluorescence [4], their operation is complex and sensitivity is average. Therefore, finding a reliable method to accurately detect CEA is very important in clinical tumor detection. With high sensitivity, quick reaction, and low background, electrochemiluminescence (ECL), a combination of electrochemical analysis and photochemical analysis has emerged as an essential method for the detection of tumor markers in blood [5–8].

In order to design a well biocompatibility sensor with superior signal conversion efficiency, luminescent groups were used to ensure the signal output of the ECL biosensor, like g-C_3N_4 [9], Ru(bpy)$_3^{2+}$ [10], polymer dots [11], quantum dots (QDs) [12], and Iridium (III) complexes [13]. As one of the most classic ECL reagents, tris(2,2′-bipyridyl)ruthenium (II) (Ru(bpy)$_3^{2+}$) and its derivatives possess super-hydrophilic properties, the stable physical and chemical properties, reversible redox, high luminous efficiency, and a long fluorescence life, which are widely used in the fields of environmental protection, food contamination control, disease diagnosis, and cell imaging [14]. Numerous nanomaterials, including mesoporous silica [15], MOF [6], and apoHSF [13] have been employed to immobilize the Ru(bpy)$_3^{2+}$ derivatives to get a strong ECL signal. However, the ion/electron long-diameter migration and diffusion constraints inhibit the electrochemical activation of the internal luminescent groups, resulting in the utilization of ECL luminescent groups is still limited [16]. It is imperative to find new carrier materials to improve the utilization rate and immobilization amount of luminescent group [17]. Metal organic layers (MOL), referred to as metal-organic framework (MOF) nanosheets or coordination nanosheets, are two-dimensional (2D) variations of MOFs that may loosen ion/electron diffusional restrictions [18]. More importantly, excitons on 2D MOFs are more easily captured by external quenchers than excitons on 3D MOFs [19]. 2D MOFs may have higher luminophores loading quantities than 3D bulk MOFs because of the larger specific surface areas and more easily accessible post-modification locations [20]. A highly stable Ru-complex-grafted 2D MOL with exceptional ECL efficiency was reported by the Xiao's group as a sensing platform for the quick and sensitive detection of Mucin 1 [16]. These results provide opportunities for light collection and fluorescence sensing using efficient exciton migration in 2D materials. Therefore, we created a new and stable Ru-complex-grafted MOL [(Hf)MOL-Ru] by immobilizing Ru(dcbpy)$_3^{2+}$ on (Hf)MOL using solvent-assisted ligand integration (SALI) due to the benefits mentioned above.

There has been an abundance of literatures since "self-enhanced ECL complex" as an ECL signal amplification strategy was first applied to the immunosensing analysis by Yuan's group in 2013 [21]. Compared to additional co-reactants, self-enhanced ECL composites can reduce electron transmission paths and energy losses by covalently attaching a suitable co-reactant to the luminophore [22]. Strong and stable ECL signals can be obtained effectively by connecting amine-rich nanomaterials with luminescent groups [16,23,24]. Among these co-reactants, poly (ethylenimine) (PEI) is an amine-rich polymer of ongoing interest as a co-reactant of the binary luminophore system [25]. Therefore, it is feasible to synthesize a functionalized 2D MOL which can effectively shorten the reaction distance between PEI and Ru(dcbpy)$_3^{2+}$. More importantly, through covalent connection, (Hf)MOL-Ru-PEI is a stable structure that can effectively prevent Ru(dcbpy)$_3^{2+}$ leakage. At the same time, loading Pd NPs onto (Hf)MOL-Ru-PEI via Pd–NH_2 could not only improve the electron transfer ability of (Hf)MOL-Ru-PEI, but also provide more active sites for the reaction of Ru(dcbpy)$_3^{2+}$ and PEI.

Quench efficiency is an important factor for the "signal on-off" immunosensor. The most commonly utilized ECL signal quenchers are Au NPs [26], ferrocene [27], H_2O_2 [28], and carbon-based nanomaterial [29]. In addition, 2D nanomaterials as luminescent carriers are beneficial to quench luminescence [19]. Previous research has shown that dopamine hydrochloride and polydopamine (PDA) containing benzoquinone or catechol units in their structure could be used as free-radical scavengers and quench the excited state of Ru(bpy)$_3^{2+}$ by energy transfer [30]. PDA can not only provide and accept electrons repeatedly for redox reactions but also has attractive qualities such as good biocompatibility, strong adhesion, and easy functionalization [31]. The $CuFe_2O_4$ nanoparticles can produce Cu^{2+} to quench the ECL of Ru(bpy)$_3^{2+}$ derivative via electron transfer as the biomolecule carriers. Through a self-polymerization process, dopamine was able to create a PDA shell on the surface of $CuFe_2O_4$, resulting in core-shell polymer material. It is worth emphasizing that PDA can adsorb MB in aqueous solution [32]. MB is a cheap and versatile indicator that is often used as a quencher for ECL analysis. As a reactant free radical scavenger and energy transfer receptor, MB can effectively inhibit the emission of luminescent groups [33]. Therefore, the combination of PDA, Cu^{2+} and MB to quench the ECL of Ru derivatives through energy and electron transfer is a feasible method.

In this work, a "signal on-off" ECL immunosensor for sensitive analysis of CEA ground on the ternary extinction effects of $CuFe_2O_4$@PDA-MB towards a self-enhanced Ru(dcbpy)$_3^{2+}$ functionalized metal-organic layer [(Hf)MOL-Ru-PEI-Pd] was prepared. Ru(dcbpy)$_3^{2+}$ and PEI covalent binding on the surface of (Hf)MOL successfully prevent the leakage of Ru(dcbpy)$_3^{2+}$ from (Hf)MOL. Shorting the reaction distance between PEI and Ru(dcbpy)$_3^{2+}$ significantly can improve the ECL efficiency of the system. At the same time, loading Pd NPs onto (Hf)MOL-Ru-PEI via Pd–NH_2 could not only improve the electron transfer ability of (Hf)MOL-Ru-PEI, but also provide more active sites for the reaction of Ru(dcbpy)$_3^{2+}$ and PEI. A potent quenching probe ($CuFe_2O_4$@PDA-MB) with ternary extinction effects was created, leading to an obvious suppression of the original ECL signal. From the UV–vis spectra of $CuFe_2O_4$@PDA-MB, a strong absorption peak at 660 nm was acquired, enabling an obvious duplication with the ECL emission spectrum of (Hf)MOL-Ru-PEI-Pd. Thus, the inner filter effect (IFE)

was triggered, leading to (Hf)MOL-Ru-PEI-Pd donors transferred energy to the $CuFe_2O_4$@PDA-MB acceptors. The IFE results from the absorption of the luminous radiation by the quenching agent [34]. It is also happened if the distance between the emitter and the re-absorber is greater than 10 nm. In a range of CEA concentrations from 0.1 pg mL^{-1} to 100 ng mL^{-1}, this immunosensor showed a wide linear response and low detection limit (20 fg mL^{-1}). This work not only provide a feasible strategy for the explanation of the ECL radiation energy transfer process, but also a hopeful method of analysis with good repeatability, high selectivity, and excellent stability for the super-sensitive detection of CEA and other clinical disease markers.

2. Experimental section

2.1. Construction of the ECL immunosensor

The used glassy carbon electrode (GCE) with diameter of 4 mm was pretreated with 0.05 μm alumina slurry and cleaned with ultra-pure water for three times to make its surface smooth. The electrode was then coated with 7 μL of (Hf)MOL-Ru-PEI-Pd (Scheme 1B). Whereafter, 7 μL of CEA captured antibodies (Ab_1, 10 μg mL^{-1}) was connected to the (Hf)MOL-Ru-PEI-Pd via a Pd–NH_2 bond. Next, surface of the electrode was carefully cleaned with PBS (1/15 mol L^{-1}, pH 7.6) to remove

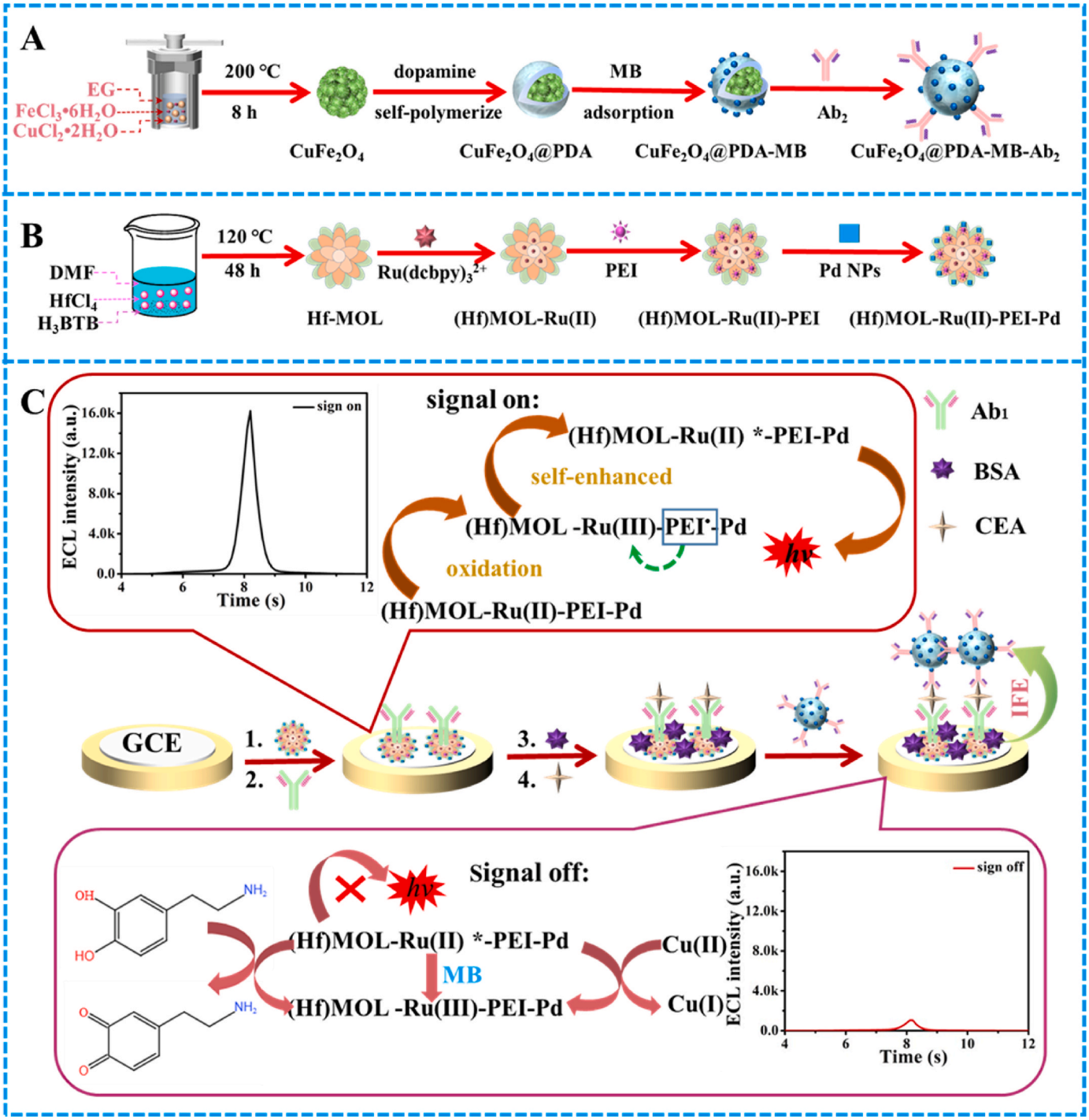

Scheme 1. (A) Diagrams depicting the stages involved in the synthesis of $CuFe_2O_4$@PDA-MB-Ab_2, (B) the synthesis steps of (Hf)MOL-Ru-PEI-Pd, (C) the manufacturing procedure for CEA sensors and potential luminescence mechanisms.

unreacted Ab_1, and 4 μL of BSA solution (0.1 wt%) was coated to block possible non-specific active binding sites. Subsequently, 7 μL of CEA antigen with concentrations ranging from 0.1 pg mL^{-1} to 100 ng mL^{-1} were coated on the sensing interface and reacted at 4 °C for 1.5 h. At last, using PBS (1/15 mol L^{-1}, pH 7.6) flush the immunosensing interface to remove unreacted of CEA, and 7 μL of detection antibody (Ab_2) bio-conjugate (Scheme 1A) was modified to the electrode. The unreacted bio-conjugate was washed by PBS after the immunological complexes were generated. The detailed preparation process of the immunosensor is shown in Scheme 1C.

2.2. ECL analysis of CEA

An MPI-E ECL analyzer (Xi'an Remex Electronic Science-Tech Co., Ltd., Xi'an, China) was carried out for CEA detection in 10 mL of PBS (pH 7.6). The concentrations of PBS used in this work are all 1/15 mol L^{-1}. Cyclic voltammetry was used to scan the electrodes in the potential range from 0 V to 1.3 V. The scan rate and the working voltage of the photomultiplier tube were set at 0.15 V s^{-1} and 800 V, respectively. With an increase in the amount of CEA, more $CuFe_2O_4$@PDA-MB-Ab_2 with an ECL signal quenching effect is coupled to the electrode, which gradually weakens the ECL signal of (Hf)MOL-Ru-PEI-Pd. The working curve was drawn according to the changes in CEA concentrations and ECL signal intensities.

3. Results and discussion

3.1. Characteristics of nanomaterials

The X-ray diffraction (XRD) patterns of (Hf)MOL-Ru-PEI show two peaks at 5.1° and 8.5°, which are the characteristic peaks of (Hf)MOL, indicating the load of $Ru(dcbpy)_3^{2+}$ and PEI did not generate new crystal phases (Fig. 1A) [35]. From the comparison with (Hf)MOL-Ru-PEI, the low intensity of diffraction peak appears at 41.6° and 46.7° which belongs to the (111) and (220) crystal planes of Pd NPs (JCPDS 46–1043), while all of the other diffraction peaks are well matched with (Hf)MOL-Ru-PEI, indicating the successful formation of the (Hf)MOL-Ru--PEI-Pd composite [36]. Furthermore, the fourier transform infrared spectroscopy (FTIR) spectra are used to demonstrate the transformation of –COOH into other functional groups (Fig. 1C) [16]. Compared with (Hf)MOL, the absorption peak of the protonated carboxylic acid group of (Hf)MOL-Ru and (Hf)MOL-Ru-PEI decreases at 1710 cm^{-1}, indicating that the carboxylic acid group of (Hf)MOL reacts with the carboxylic acid group of $Ru(dcbpy)_3^{2+}$ to form anhydride and the amino group of PEI to form a peptide bond. Compared with (Hf)MOL (1365 cm^{-1}), the absorption peak of (Hf)MOL-Ru at 1355 cm^{-1} is the C–O stretching vibration of cyclic anhydride. Therefore, through covalent connection, (Hf)MOL-Ru is a stable structure that can effectively prevent Ru $(dcbpy)_3^{2+}$ leakage. Compared with (Hf)MOL-Ru, the absorption peak of (Hf)MOL-Ru-PEI at 1320 cm^{-1} is C–N stretching vibration. The results of

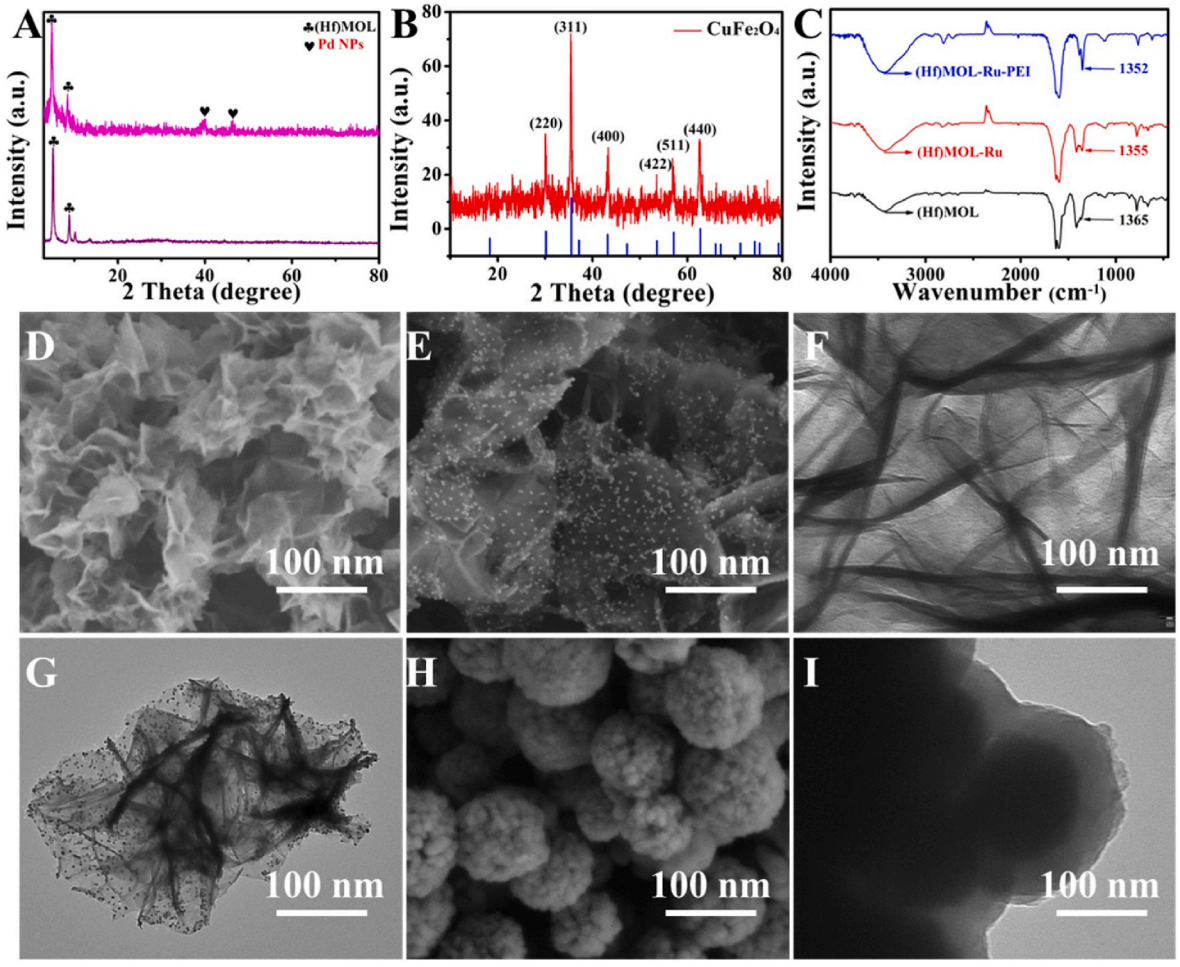

Fig. 1. (A) The XRD patterns of (Hf)MOL-Ru-PEI and (Hf)MOL-Ru-PEI-Pd. (B) The XRD patterns of $CuFe_2O_4$. (C) FTIR spectra of (Hf)MOL (black curve), (Hf)MOL-Ru (red curve), and (Hf)MOL-Ru-PEI (blue curve). The SEM of (Hf)MOL-Ru-PEI (D) and (Hf)MOL-Ru-PEI-Pd (E). The TEM of (Hf)MOL-Ru-PEI (F) and (Hf)MOL-Ru-PEI-Pd (G). (H) The SEM image of $CuFe_2O_4$. (I) The TEM image of $CuFe_2O_4$-PDA. (For interpretation of the references to color in this figure legend, the reader is referred to the Web version of this article.)

the FTIR spectra show that (Hf)MOL-Ru-PEI was prepared successfully. The appearance and structure of these nanomaterials are studied using scanning electron microscopy (SEM) and transmission electron microscopy (TEM). The SEM and TEM pictures of (Hf)MOL-Ru-PEI show that the (Hf)MOL-Ru-PEI is a wrinkled ultrathin film (Fig. 1D and F). The SEM and TEM pictures of (Hf)MOL-Ru-PEI-Pd show that a considerable number of nanoparticles were adsorbed on the surface of (Hf)MOL--Ru-PEI (Fig. 1E and G). The SEM elements mapping images and relevant energy-dispersive X-ray spectroscopy also indicate the successful synthesis of (Hf)MOL-Ru-PEI-Pd (Fig. S1). As shown in Fig. 1B, the XRD patterns of $CuFe_2O_4$ exhibits distinct peaks that are located at 30.3°, 35.4°, 43.4°, 53.7°, 57.2°, and 62.6°, corresponding to lattice planes (220), (311), (400), (422), (511), and (440), respectively (JCPDS 77-0010) [37]. The SEM image of $CuFe_2O_4$ (Fig. 1H) shows a uniformly dispersed spherical shape with a diameter of about 200 nm. As can be seen from Fig. 1I, PDA-coated $CuFe_2O_4$ is also sphere-shaped, and its rough surface has been uniformly covered with a PDA shell. These results show that $CuFe_2O_4$@PDA was prepared successfully.

3.2. Electroactive surface area for modified electrodes

The interaction region of the modified electrode is calculated to describe the state of the electrode surface. In 5 mmol L^{-1} of $[Fe(CN)_6]^{3-/4-}$ and 0.1 mol L^{-1} of KCl solution, the cyclic voltammetry test of (Hf)MOL-Ru-PEI/GCE (2.0 mg mL^{-1}) and (Hf)MOL-Ru-PEI-Pd/GCE (2.0 mg mL^{-1}) were conducted with the scanning speed ranging from 0.02 V s^{-1} to 0.38 V s^{-1}. The standard curve is plotted with the oxidation current I_{pc} as the ordinate and the power of 1/2 of the sweeping velocity as the transverse coordinate. The regression equations $I_{pc}(A) = 107.7\ v^{1/2} + 10.5$ [(Hf)MOL-Ru-PEI/GCE, Figs. S2A and S2B] and $I_{pc}(A) = 167.39.1\ v^{1/2} + 13.8$ [(Hf)MOL-Ru-PEI-Pd/GCE, Fig. 2A and C] show that diffusion is the only influence factor of electrode surface. According to the Randles-Sevcik equation ($I_{pc} = 269000A{\cdot}D^{1/2}{\cdot}n^{3/2}{\cdot}v^{1/2}{\cdot}c$), where $c = 5$ mmol L^{-1}; $n = 1$; v is the cyclic voltammetry scan rate (V s^{-1}); D is the diffusion coefficient ($D = 6.70 \pm 0.02 \times 10^{-6}$ cm^2 s^{-1} at 25 °C); A is the effective electroactive surface area (cm^2); and I_{pc} is the peak current. The calculated effective electrochemical active area of [(Hf)MOL-Ru-PEI-Pd] (0.21 cm^2) is 0.62 times larger than the actual area of (Hf)MOL-Ru-PEI (0.13 cm^2) [38]. Therefore, the catalytic sites on the (Hf)MOL-Ru-PEI-Pd were increased. ECL and cyclic voltammogram (CV) of (Hf)MOL-Ru-PEI-Pd and (Hf)MOL-Ru-PEI were studied in PBS solution (pH 7.6). It can be seen from Fig. 2B that the CV of (Hf)MOL-Ru-PEI-Pd has an oxidation peak at 1.06 V, while (Hf)MOL-Ru-PEI does not. Compared with (Hf)MOL-Ru-PEI (1.17 V), the luminescent potential of (Hf)MOL-Ru-PEI-Pd (1.05 V) was 0.12 V earlier, indicated that Pd NPs has a co-reaction promoting effect to (Hf)MOL-Ru-PEI system [8]. These findings suggest that Pd NPs can provide more active sites for the reaction of $Ru(dcbpy)_3^{2+}$ and PEI.

3.3. ECL mechanism of the (Hf)MOL-Ru-PEI-Pd

In order to demonstrate the superiority of the (Hf)MOL-Ru-PEI-Pd, control experiments were conducted. Compared with the ECL signal of the (Hf)MOL-Ru-PEI/GCE (Fig. 2D, curve d), the ECL signal of the (Hf)MOL-Ru-PEI-Pd modified electrode (Fig. 2D, curve a) increased by 0.3 times. This finding shows that Pd NPs can improve the ECL emission of $Ru(dcbpy)_3^{2+}$. As well, we analyzed how PEI affected the ECL of modified electrodes containing (Hf)MOL-Ru in different buffers by detecting ECL responses. The ECL signal strength of the (Hf)MOL-Ru modified electrode with PEI (Fig. 2D, curve b) as a co-reactant is 2.7 times than that of N,N-Dibutyl-2-hydroxyethylamine (DBAE) as a co-reactant (Fig. 2D, curve c), so PEI as a co-reactant of (Hf)MOL-Ru is a better choice. As clearly observed from Fig. 3A, either covalently binding the reactant PEI to the luminescent functionalized (Hf)MOL-Ru or adding it to the working buffer has a major impact on the ECL emission of (Hf)MOL-Ru. In addition, the time required for the (Hf)MOL-Ru-PEI (Fig. 3A, curve a) to reach the maximum ECL signal is faster than that of (Hf)MOL-Ru with PEI added to the electrolyte (Fig. 3A, curve b), indicating that the (Hf)MOL-Ru-PEI composite can effectively reduce the energy loss of Ru $(dcbpy)_3^{2+}$ and improve the ECL efficiency because of the short charge and energy transport distance provided by the intramolecular rapid reaction.

The fluorescence (FL) and ECL spectra of (Hf)MOL-Ru-PEI-Pd were obtained using the same setup used for the spectroscopic study (Fig. 3B).

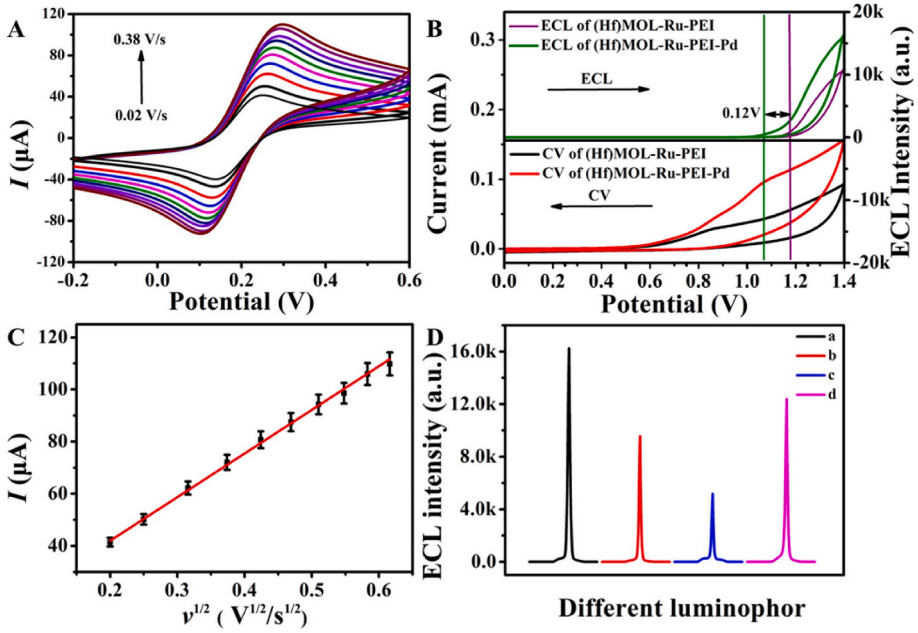

Fig. 2. (A) CV of (Hf)MOL-Ru-PEI-Pd modified electrodes at different scanning speeds (0.02 V s^{-1}–0.38 V s^{-1}). (B) The ECL and CV spectra of (Hf)MOL-Ru-PEI-Pd and (Hf)MOL-Ru-PEI were studied in PBS solution (pH 7.6). (C) The linear relationship of (Hf)MOL-Ru-PEI-Pd modified electrodes at different scanning speeds (0.02 V s^{-1}–0.38 V s^{-1}). (D) The ECL intensity comparison of (Hf)MOL-Ru-PEI-Pd/GCE (a), (Hf)MOL-Ru/GCE containing 30 μL of PEI (b), (Hf)MOL-Ru/GCE containing 30 μL of DBAE (c), and (Hf)MOL-Ru-PEI/GCE (d) were measured in 10 mL of PBS.

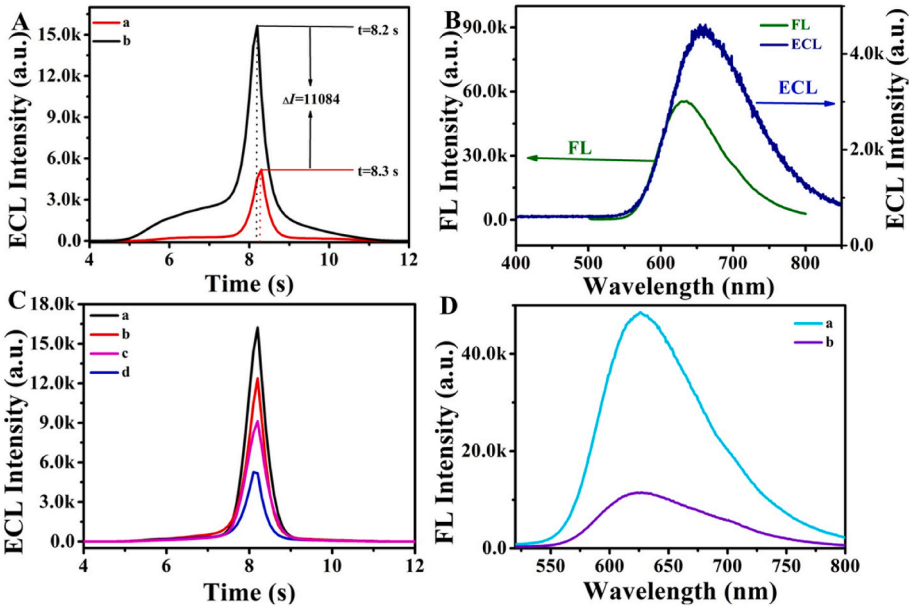

Fig. 3. (A) The ECL time-intensity curve of (Hf)MOL-Ru-PEI/GCE in 10 mL of PBS (pH 7.6) (a) and (Hf)MOL-Ru/GCE in 10 mL of PBS (pH 7.6) containing 30 μL of PEI (b). (B) The normalized ECL-FL intensity spectra of (Hf)MOL-Ru-PEI-Pd were measured by the same spectrophotometer. (C) Comparison of the quenching effects of several Ab_2 bioconjugates: (a) Ab_2/CEA/BSA/Ab_1/(Hf)MOL-Ru-PEI-Pd/GCE, (b) $CuFe_2O_4$/Ab_2/CEA/BSA/Ab_1/(Hf)MOL-Ru-PEI-Pd/GCE, (c) $CuFe_2O_4$@PDA-Ab_2/CEA/BSA/Ab_1/(Hf)MOL-Ru-PEI-Pd/GCE, (d) $CuFe_2O_4$@PDA-MB-Ab_2/CEA/BSA/Ab_1/(Hf)MOL-Ru-PEI-Pd. (D) The FL spectra of (Hf)MOL-Ru-PEI-Pd (a) and (Hf)MOL-Ru-PEI-Pd contained 1 mg mL^{-1} of $CuFe_2O_4$@PDA-MB (b).

As can be seen from the FL spectra of (Hf)MOL-Ru-PEI-Pd, the FL has peaks at 640 nm. The ECL emission peaks at 660 nm and shows a red shift of 20 nm compared to the FL, so the excited states of (Hf)MOL-Ru-PEI-Pd may be generated by a mechanism of surface state transitions at lower energies than the band gap [39]. As a result, more defects in the loaded material favor the generation of excited-state species. According to the literature review [16,22,25,40], the possible ECL mechanism of (Hf)MOL-Ru-PEI-Pd is as follows: First of all, Ru(II) and PEI in (Hf)MOL-Ru(II)-PEI-Pd lose electrons to become Ru(III) complexes and $PEI^{\bullet+}$ (equation (1)). At the same time, $PEI^{\bullet+}$ deprotonation to form $PEI^{\bullet}$, which can undergo an intramolecular reaction with Ru(III) to generate excited (Hf)MOL-Ru(II)*-PEI-Pd (equations (2) and (3)). (Hf)MOL-Ru(II)*-PEI-Pd release energy produces an ECL signal (equation (4))

$$(Hf)MOL-Ru(II)-PEI-Pd-2e^{-} \rightarrow (Hf)MOL-Ru(III)-PEI^{\bullet+}-Pd \quad (1)$$

$$(Hf)MOL-Ru(III)-PEI^{\bullet+}-Pd-H^{+} \rightarrow (Hf)MOL-Ru(III)-PEI^{\bullet}-Pd \quad (2)$$

$$(Hf)MOL-Ru(III)-PEI^{\bullet}-Pd \rightarrow (Hf)MOL-Ru(II)*-PEI-Pd \quad (3)$$

$$(Hf)MOL-Ru(II)*-PEI-Pd \rightarrow (Hf)MOL-Ru(II)-PEI-Pd+hv \quad (4)$$

$$(Hf)MOL-Ru(II)*-PEI-Pd+Cu^{2+} \rightarrow (Hf)MOL-Ru(III)-PEI-Pd+Cu^{+} \quad (5)$$

$$PDA-2e^{-} \rightarrow PDA^{2+} \quad (6)$$

$$(Hf)MOL-Ru(II)*-PEI-Pd+PDA^{2+} \rightarrow (Hf)MOL-Ru(III)-PEI-Pd+PDA \quad (7)$$

3.4. Quenching mechanism of $CuFe_2O_4$@PDA-MB

At the same time, the quenching efficiency of the probe seriously affects the sensitivity of the immunosensor. As is depicted in Fig. 3C, with only Ab_2, the ECL signal of the system is 17000 a.u. (curve a). A weak ECL signal of around 13000 a.u. was observed when $CuFe_2O_4$ and Ab_2 were drop on the electrode because Cu^{2+} might prevent excited state $Ru(dcbpy)_3^{2+}$ emission via electron transport (curve b) (equation (5)) [41,42]. The excited state of (Hf)MOL-Ru-PEI-Pd may be quenched by benzoquinone or catechol functional groups in PDA by electron and energy transfer (equation (6)), which leads to a clear reduction in ECL emission by $CuFe_2O_4$@PDA-Ab_2 applied to the electrode (curve c). In order to further understand the quenching efficiency of $CuFe_2O_4$@PDA-MB on the excited state (Hf)MOL-Ru-PEI-Pd, the fluorescence emission spectra of the mixed solution of $CuFe_2O_4$@PDA-MB and (Hf)MOL-Ru-PEI-Pd were tested (Fig. 3D). It can be seen that the maximum fluorescence emission wavelength of (Hf)MOL-Ru-PEI-Pd is 640 nm and the fluorescence intensity is 48000 a.u (Fig. 3D, curve a). The fluorescence intensity of (Hf)MOL-Ru-PEI-Pd obviously decreased after being mixed with $CuFe_2O_4$@PDA-MB (Fig. 3D, curve b), demonstrating that $CuFe_2O_4$@PDA-MB was able to prevent (Hf)MOL-Ru-PEI-Pd from emitting fluorescence (equation (7)). Additionally, the ECL emission spectra of (Hf)MOL-Ru-PEI-Pd and the UV–vis absorption spectra of $CuFe_2O_4$@PDA-MB were investigated. The purple curve in Fig. 4A shows that the greatest emission in the ECL spectra of (Hf)MOL-Ru--PEI-Pd occurred around 660 nm. At the same time, a stronger UV–vis absorption peak (664 nm) was acquired from MB and $CuFe_2O_4$@PDA-MB, whereas PDA, $CuFe_2O_4$, and $CuFe_2O_4$@PDA do not. Moreover, the ECL emission spectrum of (Hf)MOL-Ru-PEI-Pd overlaps obviously with the UV–vis absorption spectrum of $CuFe_2O_4$@PDA-MB (Fig. 4A, blue curve), while PDA, $CuFe_2O_4$, and $CuFe_2O_4$@PDA have almost none. These results suggest that there may be an energy transfer between (Hf)MOL-Ru-PEI-Pd and $CuFe_2O_4$@PDA-MB, and that the main receptor for this energy transfer is MB. Because the UV–vis absorption spectra of $CuFe_2O_4$@PDA-MB significantly overlapped with the ECL spectrum of (Hf)MOL-Ru-PEI-Pd from 500 to 800 nm (Fig. 4A) and the distance between $CuFe_2O_4$@PDA-MB and (Hf)MOL-Ru-PEI-Pd was assumed to be

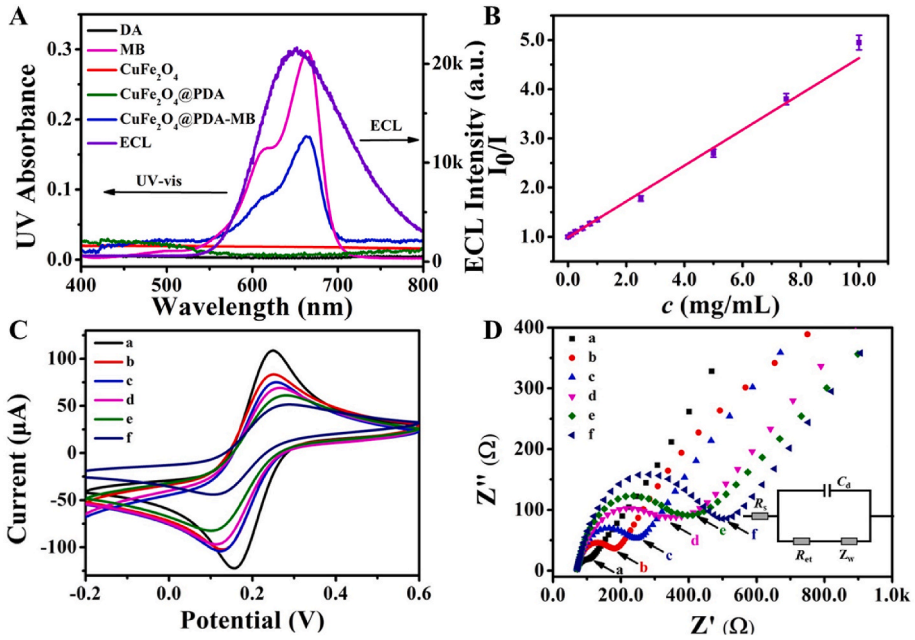

Fig. 4. (A) The ECL spectra of (Hf)MOL-Ru-PEI-Pd and the UV–vis spectra of $CuFe_2O_4$, MB, PDA, $CuFe_2O_4$@PDA, $CuFe_2O_4$@PDA-MB. (B) Stern-Volmer quenching intensity plot of (Hf)MOL-Ru-PEI-Pd contained 0, 0.10, 0.25, 0.50, 0.75, 1.00, 2.50, 5.00, 7.50, and 10.00 mg mL^{-1} of $CuFe_2O_4$@PDA-MB in 10 mL of PBS (pH 7.6). (C) The CV curves and EIS responses (D) for (a) bare GCE, (b) GCE/(Hf)MOL-Ru-PEI-Pd, (c) GCE/(Hf)MOL-Ru-PEI-Pd/Ab_1, (d) GCE/(Hf)MOL-Ru-PEI-Pd/Ab_1/BSA, (e) GCE/(Hf)MOL-Ru-PEI-Pd/Ab_1/BSA/CEA, (f) GCE/(Hf)MOL-Ru-PEI-Pd/Ab_1/BSA/CEA/$CuFe_2O_4$@PDA-MB-Ab_2.

less than 10 nm, the fluorescence resonance energy transfer (FRET) theory was first applied to demonstrate the quenching process. According to previous works, the Förster radius R_0 was calculated to be 13.44 nm (detailed calculation in Supplementary Material). In this sandwich CEA immunosensor, the distance between (Hf)MOL-Ru--PEI-Pd and $CuFe_2O_4$@PDA-MB is greater than 10 nm, so the quenching of (Hf)MOL-Ru-PEI-Pd by MB cannot be explained by resonance energy transfer [43]. Thus, the quenching mechanism of (Hf)MOL-Ru-PEI-Pd by MB was first considered by IFE. In the IFE theory, (Hf)MOL-Ru-PEI-Pd acts as the energy donor, and $CuFe_2O_4$@PDA-MB acts as the energy acceptor. Since IFE mainly comes from the MB of $CuFe_2O_4$@PDA-MB, the quenching efficiency of the MB on (Hf)MOL-Ru-PEI-Pd was investigated separately. The ECL of (Hf)MOL-Ru-PEI-Pd was gradually decreased upon the continuous addition of MB in solution after removing the quenching effect of $CuFe_2O_4$@PDA. The results show that MB has better quenching ability of ECL in (Hf)MOL-Ru-PEI-Pd (Fig. S3).

The quenching effect of the quenching agent has been well documented and can be evaluated using the quenching rate constant (k_q) according to Stern-Volmer equation ($I_0/I = 1 + k_q\tau_0\cdot[Q] + K_{sv}\cdot[Q]$) [43,44]. In this equation, I_o is the ECL emission intensity in the absence of quenching agent; I is the ECL emission intensity in the presence of a quenching agent; K_{sv} is the Stern-Volmer constant; k_q is the quenching rate constant; τ_0 is fluorescence lifetime [the τ_0 of $Ru(dcbpy)_3^{2+}$ is 1080 ns]; and [Q] is the concentration of quenching agent. We measured the ECL intensity of (Hf)MOL-Ru-PEI-Pd/GCE in the presence of $CuFe_2O_4$@PDA-MB at different concentrations (0, 0.10, 0.25, 0.50, 0.75, 1.00, 2.50, 5.00, 7.50, and 10.00 mg mL^{-1}) (Fig. 4B and Fig. S4). With I/I_o as the vertical coordinate and the concentration of $CuFe_2O_4$@PDA-MB as the horizontal coordinate, the slope of the working curve obtained is 0.36, so the K_{sv} is 0.36 L g^{-1}, and k_q is 3.4×10^5 L $g^{-1}\cdot s^{-1}$. The large k_q value indicates highly extinction capability of $CuFe_2O_4$@PDA-MB, which increases the possibility of constructing signal quenched ECL immunosensors [45].

3.5. Characterization of the ECL immunosensor

The successful manufacturing of the immunosensor was demonstrated using CV in Fig. 4C. In 2.5 mmol L^{-1} of $[Fe(CN)_6]^{3-/4-}$ solution, bare GCE showed a distinct reversible redox peak (Fig. 4C, curve a). The electrical conductivity may be reduced after (Hf)MOL-Ru-PEI-Pd coated on electrode, so a noticeably decreased peak current was seen (Fig. 4C, curve b). At the same time, the oxidation and reduction peak currents gradually dropped after the immobilization of Ab_1, BSA, and CEA (Fig. 4C, curves c, d, and e), due to the poor electrical conductivity of proteins. The addition of $CuFe_2O_4$@PDA-MB-Ab_2 resulted in a further reduction in redox current intensity, demonstrating the efficacy of its conjugation with CEA (Fig. 4C, curve f). To further verify the successful fabrication of the immunosensor, electrochemical impedance spectroscopy (EIS) was carried out. In the EIS experiments, our instrument parameters of frequency range and amplitude were set as 100 mHz–100 kHz and 5 mV respectively. The bias voltage remained the default 0 V. The buffer solution used in the tests was a kind of mixed solution containing 2.5 mmol L^{-1} $K_3[Fe(CN)_6]$, 2.5 mmol L^{-1} $K_4[Fe(CN)_6]$ and 0.1 mol L^{-1} KCl. The specific process is as follows: oxidation reaction: $Fe^{2+} - e^- \rightarrow Fe^{3+}$; reduction reaction: $Fe^{3+} + e^- \rightarrow Fe^{2+}$. Due to the (Hf)MOL-Ru-PEI weak electrical conductivity of composite material, as shown in Fig. 4D, the electron transfer resistance (Ret) of (Hf)MOL-Ru-PEI-Pd (Fig. 4D, curve b) was elevated in comparison to that of bare GCE (Fig. 4D, curve a). The impedance increased after the electrode was coated with Ab_1, BSA, and CEA (Fig. 4D, curves c, d, and e), indicating that the biomaterials were successfully modified on the electrode. Additionally, the impedance value increased with the addition of the $CuFe_2O_4$@PDA-MB-Ab_2 (Fig. 4D, curve f). The experimental results of CV and EIS characterizations proved that the immunosensor was successfully built.

3.6. Optimization experimental conditions

The effects of experimental factors such the quantity of (Hf)MOL-Ru-PEI-Pd, the duration of $CuFe_2O_4$@PDA-MB-Ab_2 incubation, and impact of PBS (pH value) were all investigated [46,47]. The concentration of (Hf)MOL-Ru-PEI-Pd was tuned in order to produce the high ECL efficiency of the luminophore, and the outcome is shown in Fig. 5A. The ECL intensity significantly rose as (Hf)MOL-Ru-PEI-Pd concentration

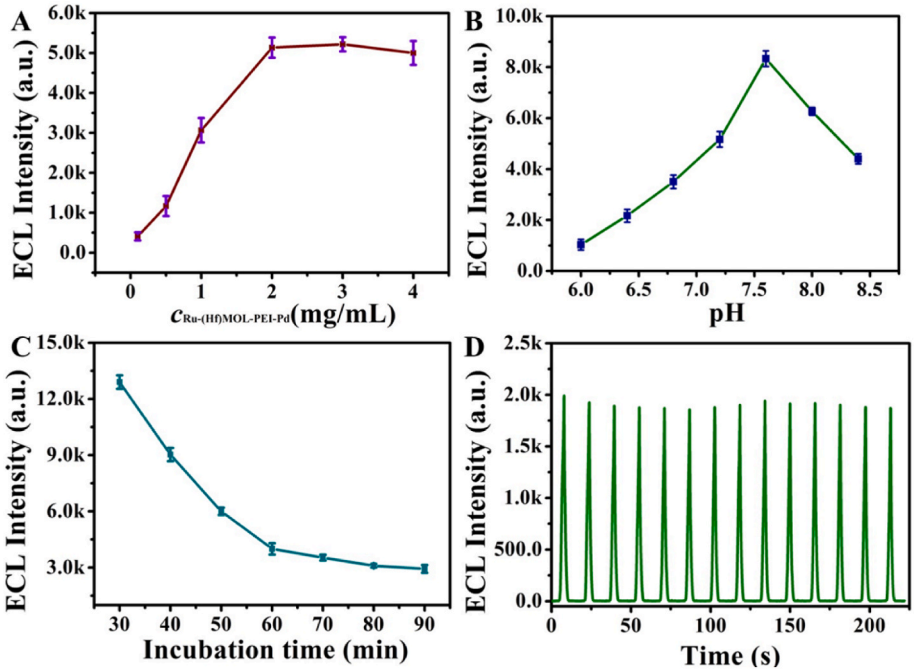

Fig. 5. (A) The optimization of concentration of (Hf)MOL-Ru-PEI-Pd and (B) the pH value of PBS. (C) The optimization of incubation time of Ab_2 bioconjugates. (D) Stability of the sensor at 100 ng mL^{-1} of CEA.

increased from 0.5 mg mL^{-1} to 4 mg mL^{-1}, but it ultimately stabilized with further enhancement of (Hf)MOL-Ru-PEI-Pd content, likely because the higher content of (Hf)MOL-Ru-PEI-Pd is not conducive to electron transport. Therefore, the ideal (Hf)MOL-Ru-PEI-Pd concentration was 2 mg mL^{-1}, which can prevent reagent waste and obtain good ECL efficiency. In addition, PBS with a pH range of 6.0–8.4 was selected to investigate the effects of ECL intensity. Evidently, pH 7.6 was chosen for improved bioactivities of biomolecule and a greater ECL response of the immunosensor. (Fig. 5B). The binding amount of the quenched probe seriously affects the sensitivity of the sensor, so it is necessary to optimize the incubation time of the secondary antibody marker (Fig. 5C). When the incubation time increased from 30 to 90 min, the ECL intensity experienced a dramatic decline before plateauing. In light of this, a suitable incubation period of 90 min was chosen for the subsequent experiment.

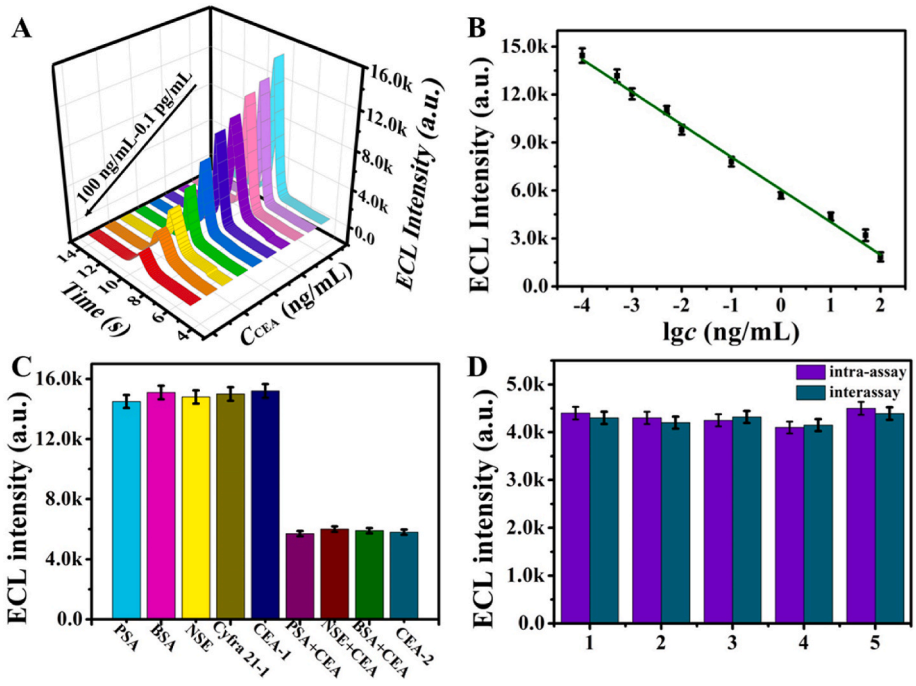

Fig. 6. (A) The ECL time-intensity curve and (B) sensor operating curve of CEA concentration gradient from 0.1 pg mL^{-1} to 100 ng mL^{-1}. The conditions were performed in PBS (10 mL, pH 7.6) (Error bars: SD, n = 3). (C) The selectivity of the immunosensor (the sensor was used to detect 5 ng mL^{-1} PSA, BSA, NSE, CYFRA 21-1, and the mixtures of these interferors with 1 ng mL^{-1} CEA). (D) Intra-assay and inter-assay of electrodes in the same batch. Error bars: ±standard deviation (SD), n = 5.

3.7. Analytical performance of the ECL immunosensor

In order to obtain the best analytical performance of synergistic quenching type immunosensor (Because the Cu^{2+} and PDA of $CuFe_2O_4$@PDA-MB in the system will have a negative effect on the excited (Hf)MOL-Ru*-PEI-Pd (dynamic quenching effect), while MB realizes the ECL signal attenuation of (Hf)MOL-Ru-PEI-Pd through IFE), a series of CEA concentrations were selected to plot the working curve under optimal experimental conditions [48,49]. As shown in Fig. 6A, ECL intensity gradually decreased with increasing CEA concentrations. Fig. 6B shows a linear relationship between ECL intensity and the logarithm of CEA concentration from 0.1 pg mL^{-1} to 100 ng mL^{-1}. The curve can be well described by the equation: $y = 6054.5–2035.5$ lg c, where c is the concentration of CEA in the detected sample, and y is the ECL intensity corresponding to concentration of CEA. The limit of detection (LOD) was calculated to be 20 fg mL^{-1} (in accordance with the definition of LOD provided by IUPAC), and the square of correlation coefficient (R^2) was 0.99. Due to the outstanding ECL property of (Hf)MOL-Ru-PEI-Pd and the extremely effective quenching ability of $CuFe_2O_4$@PDA-MB, the analytical performances were superior than those of the literatures listed in Table 1.

3.8. Repeatability, stability, and selectivity of the immunosensor

In order to evaluate the practical application capability of the immunosensor, selectivity, repeatability, and stability are investigated separately. Common cancer markers, such as NSE, PSA, CYFRA 21-1, and BSA were used as interfering substances to explore the selectivity of the immunosensor (Fig. 6C). When 5 ng mL^{-1} of NSE, PSA, CYFRA 21-1, and BSA were detected separately, the ECL signal of the sensor is fundamentally unchanged. The ECL intensity was consistent with 1 ng mL^{-1} of CEA when it was mixed with 5 ng mL^{-1} of PSA, BSA, and NSE separately. The laboratory finding shows that the immunosensor has excellent selectivity. The reproducibility of CEA immunosensors was explored with intra- and inter-assay precision. The intra-assay accuracy was determined by evaluating one CEA level on five reduced duplicate readings. Five immunosensors were used to detect CEA to determine the inter-assay accuracy. The intra- and inter-assay variability coefficients obtained from CEA at 1 ng mL^{-1} were 3.5 % and 4.7 %, respectively. Both the intra- and inter-assay precision indicates that immunosensors have excellent reproducibility (Fig. 6D) [57]. The operational stability of sensors is an influential factor affecting the practical applications of immunosensors. As shown in Fig. 5D, after the modification of 100 ng mL^{-1} of CEA and successful incubation of $CuFe_2O_4$@PDA-MB, the modified electrodes exhibit a strong and stable ECL response under 0–1.3 V scanning and an RSD of 2.0 % after 14 consecutive cycles. This results show that the sensor is stable. At the same time, the ECL response of the sensor stored at 4 °C for a long time shows acceptable storage stability (Fig. S5) [58].

3.9. Actual sample detection and analysis

The use of real serum samples for analytical testing can accurately reflect the potential of biosensors [59–62]. CEA is a typical cancer marker. In this work, CEA was used as the target analyses to detect and analyze CEA (2.0 ng mL^{-1}) in human serum samples by the labeled recovery method, and the recovery range was as follows: 96.8%–105.5 % (n = 5); RSD ranged from 2.9% to 3.1 % (Table S1). This result indicates that the constructed sensor has acceptable accuracy and is expected to be developed for clinical applications.

4. Conclusion

In summary, a “signal on-off” type ECL immunosensor was constructed for CEA analysis ground on ternary extinction effects of $CuFe_2O_4$@PDA-MB towards self-enhanced (Hf)MOL-Ru-PEI-Pd complexes. The prepared immunosensor has the following fascinating characteristics. Firstly, the high ECL efficiency of (Hf)MOL-Ru-PEI-Pd originated from the dual intramolecular self-catalysis, including intramolecular co-reaction between PEI and $Ru(dcbpy)_3^{2+}$, which generate a strong initial ECL signal after loading Pd NPs. Besides, $CuFe_2O_4$@PDA-MB-Ab_2 quenches the excited states of $Ru(dcbpy)_3^{2+}$ by PDA, Cu^{2+}, and MB via energy and electron transfer. In particular, the ECL quenching of $Ru(dcbpy)_3^{2+}$ by MB was firstly explained by the inner filter effect quenching mechanism. Under the optimum experimental conditions, the proposed sensor had good linearity with the CEA concentration of 0.1 pg mL^{-1}–100 ng mL^{-1}, and a detection limit of 20 fg mL^{-1} (S/N = 3) was obtained. The prepared sensor has high selectivity, good reproducibility, and stability offered an efficient strategy to estimate CEA and also provided a candidate for quantitative analysis of many other kinds of tumor markers.

Table 1
The comparison of CEA detection methods.

Detecting method	Materials	Linear range (pg mL^{-1})	Detection limit (pg mL^{-1})	References
Electrochemical Methods	Au NPs/COFTFPB-Thi	1.1 × 10^2–8 × 10^4	34	[50]
Electrochemical Methods	MXC-Fe_3O_4–Ru	1–4 × 10^6	0.62	[51]
PEC	Ag/MoO_3–Pd	1 × 10^2–1 × 10^4	26	[52]
PL	Nd doped $NaYF_4$	1.80 × 10^2–3.2 × 10^5	370	[53]
ECL	Ru–Si-NPs and Au NPs	5–5 × 10^5	1.6	[54]
ECL	AuNPs@Ir–Zr-MOL	1–1 × 10^5	0.2	[55]
ECL	Ru@NH_2-MIL-88 (Fe) and Au@MoS_2	1–1 × 10^5	38.9	[56]
This work	(Hf)MOL-Ru-PEI-Pd and $CuFe_2O_4$@PDA-MB	1.0 × 10^{-1}–1 × 10^5	0.02	

CRediT authorship contribution statement

Xiang Ren: Supervision, Funding acquisition, Project administration, Writing – review & editing, Formal analysis. **Zuoxun Xie:** Conceptualization, Data curation, Writing – original draft, Formal analysis. **Huan Wang:** Methodology, Data curation. **Lijun Wang:** Methodology, Writing – review & editing. **Zhongfeng Gao:** Methodology, Writing – review & editing. **Hongmin Ma:** Methodology, Writing – review & editing. **Nuo Zhang:** Methodology, Formal analysis. **Dawei Fan:** Methodology, Data curation. **Qin Wei:** Writing – review & editing, Funding acquisition, Formal analysis. **Huangxian Ju:** Writing – review & editing, Funding acquisition, Formal analysis.

Declaration of competing interest

The authors declare that they have no known competing financial interests or personal relationships that could have appeared to influence the work reported in this paper.

Data availability

No data was used for the research described in the article.

Acknowledgment

This study was supported by the National Natural Science Foundation of China (No. 22204059, No. 22204060, No. 22274062), the Natural Science Foundation of Shandong Province (No. ZR2021QB120, ZR2022QB021), the Foundation of Yunnan Key Laboratory of Rural Energy Engineering (Yunnan Normal University), the Special Foundation for Taishan Scholar Professorship of Shandong Province (Prof. Q. Wei), Talent Introduction and Training Program for Youth Innovation teams in Colleges and universities of Shandong Province.

Appendix A. Supplementary data

Supplementary data to this article can be found online at https://doi.org/10.1016/j.aca.2023.342091.

References

[1] R.A. Miksad, N.J. Meropol, Carcinoembryonic antigen-still more to learn from the real world, JAMA Oncol. 4 (3) (2018) 315–316, https://doi.org/10.1001/jamaoncol.2017.4408.

[2] H. Liang, Y. Luo, Y. Li, Y. Song, L. Wang, An immunosensor using electroactive COF as signal probe for electrochemical detection of carcinoembryonic antigen, Anal. Chem. 94 (13) (2022) 5352–5358, https://doi.org/10.1021/acs.analchem.1c05426.

[3] L. Lu, X. Hu, R. Zeng, Q. Lin, X. Huang, Q. Wei, D. Tang, D. Knopp, Ag/MoO_3-Pd-mediated gasochromic reaction: an efficient dual-mode photoelectrochemical and photothermal immunoassay, Biosens. Bioelectron. 230 (2023), 115267, https://doi.org/10.1016/j.bios.2023.115267.

[4] Z. Song, Y. Suo, S. Duan, S. Zhang, L. Liu, B. Chen, Z. Cheng, NIR-II fluorescent nanoprobe-labeled lateral flow biosensing platform: a high-performance point-of-care testing for carcinoembryonic antigen, Biosens. Bioelectron. 224 (2023), 115063, https://doi.org/10.1016/j.bios.2023.115063.

[5] Y. Zhao, L. Bouffier, G. Xu, G. Loget, N. Sojic, Electrochemiluminescence with semiconductor (nano)materials, Chem. Sci. 13 (9) (2022) 2528–2550, https://doi.org/10.1039/d1sc06987j.

[6] X. Li, X. Ren, L. Yang, W. Wang, D. Fan, X. Kuang, X. Sun, Q. Wei, H. Ju, Ru $(dcbpy)_3^{2+}$-functionalized γ-cyclodextrin metal-organic frameworks as efficient electrochemiluminescence tags for the detection of CYFRA21-1 in human serum, Sens. Actuators, B 378 (2023), 133152, https://doi.org/10.1016/j.snb.2022.133152.

[7] J.H. Zhang, M. Liu, F. Zhou, H.L. Yan, Y.G. Zhou, Homogeneous electrochemical immunoassay using an aggregation-collision strategy for alpha-fetoprotein detection, Anal. Chem. 95 (5) (2023) 3045–3053, https://doi.org/10.1021/acs.analchem.2c05193.

[8] L. Hu, Y. Wu, M. Xu, W. Gu, C. Zhu, Recent advances in co-reaction accelerators for sensitive electrochemiluminescence analysis, Chem. Commun. 56 (75) (2020) 10989–10999, https://doi.org/10.1039/d0cc04371k.

[9] C. Song, X. Li, L. Hu, T. Shi, D. Wu, H. Ma, Y. Zhang, D. Fan, Q. Wei, H. Ju, Quench-type electrochemiluminescence immunosensor based on resonance energy transfer from carbon nanotubes and Au-Nanoparticles-Enhanced g-C_3N_4 to CuO@polydopamine for procalcitonin detection, ACS Appl. Mater. Interfaces 12 (7) (2020) 8006–8015, https://doi.org/10.1021/acsami.9b22782.

[10] X. Dong, G. Zhao, L. Liu, X. Li, Q. Wei, W. Cao, Ultrasensitive competitive method-based electrochemiluminescence immunosensor for diethylstilbestrol detection based on $Ru(bpy)_3^{2+}$ as luminophor encapsulated in metal-organic frameworks UiO-67, Biosens. Bioelectron. 110 (2018) 201–206, https://doi.org/10.1016/j.bios.2018.03.066.

[11] L. Li, S. Yu, J. Wu, H. Ju, Regulation of target-activated CRISPR/Cas12a on surface binding of polymer dots for sensitive electrochemiluminescence DNA analysis, Anal. Chem. 95 (18) (2023) 7396–7402, https://doi.org/10.1021/acs.analchem.3c01521.

[12] G. Yang, Y. He, J. Zhao, S. Chen, R. Yuan, Ratiometric electrochemiluminescence biosensor based on Ir nanorods and CdS quantum dots for the detection of organophosphorus pesticides, Sens. Actuators, B 341 (2021), 130008, https://doi.org/10.1016/j.snb.2021.130008.

[13] L. Yang, X. Sun, D. Wei, H. Ju, Y. Du, H. Ma, Q. Wei, Aggregation-Induced electrochemiluminescence bioconjugates of apoferritin-encapsulated iridium(III) complexes for biosensing application, Anal. Chem. 93 (3) (2021) 1553–1560, https://doi.org/10.1021/acs.analchem.0c03877.

[14] J. Hu, Y. Zhang, Y. Chai, R. Yuan, Boron carbon nitride nanosheets-Ru nanocomposite self-enhancement electrochemiluminescence emitter with a three-dimensional DNA network structure as a signal amplifier for ultrasensitive detection of TK1 mRNA, Anal. Chem. 94 (32) (2022) 11345–11351, https://doi.org/10.1021/acs.analchem.2c02110.

[15] W. Zhang, H. Xiong, M. Chen, X. Zhang, S. Wang, Surface-enhanced molecularly imprinted electrochemiluminescence sensor based on Ru@SiO_2 for ultrasensitive detection of fumonisin B_1, Biosens. Bioelectron. 96 (2017) 55–61, https://doi.org/10.1016/j.bios.2017.04.035.

[16] G.B. Hu, C.Y. Xiong, W.B. Liang, Y. Yang, L.Y. Yao, W. Huang, W. Luo, R. Yuan, D. R. Xiao, Highly stable Ru-complex-grafted 2D metal-organic layer with superior electrochemiluminescent efficiency as a sensing platform for simple and ultrasensitive detection of mucin 1, Biosens. Bioelectron. 135 (2019) 95–101, https://doi.org/10.1016/j.bios.2019.03.026.

[17] B. Mohan, S. Kumar, V. Kumar, T. Jiao, H.K. Sharma, Q. Chen, Electrochemiluminescence metal-organic frameworks biosensing materials for detecting cancer biomarkers, TrAC, Trends Anal. Chem. 157 (2022), 116735, https://doi.org/10.1016/j.trac.2022.116735.

[18] H. Zhong, M. Wang, G. Chen, R. Dong, X. Feng, Two-dimensional conjugated metal-organic frameworks for electrocatalysis: opportunities and challenges, ACS Nano 16 (2) (2022) 1759–1780, https://doi.org/10.1021/acsnano.1c10544.

[19] L. Cao, Z. Lin, W. Shi, Z. Wang, C. Zhang, X. Hu, C. Wang, W. Lin, Exciton migration and amplified quenching on two-dimensional metal-organic layers, J. Am. Chem. Soc. 139 (20) (2017) 7020–7029, https://doi.org/10.1021/jacs.7b02470.

[20] Y. Yang, G.B. Hu, W.B. Liang, L.Y. Yao, W. Huang, R. Yuan, D.R. Xiao, A highly sensitive self-enhanced aptasensor based on a stable ultrathin 2D metal-organic layer with outstanding electrochemiluminescence property, Nanoscale 11 (20) (2019) 10056–10063, https://doi.org/10.1039/c9nr00860h.

[21] Y. Zhuo, N. Liao, Y.Q. Chai, G.F. Gui, M. Zhao, J. Han, Y. Xiang, R. Yuan, Ultrasensitive apurinic/apyrimidinic endonuclease 1 immunosensing based on self-enhanced electrochemiluminescence of a Ru(II) complex, Anal. Chem. 86 (2) (2014) 1053–1060, https://doi.org/10.1021/ac403019e.

[22] H. Wang, Y. Yuan, Y. Chai, R. Yuan, Self-enhanced electrochemiluminescence immunosensor based on nanowires obtained by a green approach, Biosens. Bioelectron. 68 (2015) 72–77, https://doi.org/10.1016/j.bios.2014.12.016.

[23] L. Luo, S. Ma, L. Li, X. Liu, J. Zhang, X. Li, D. Liu, T. You, Monitoring zearalenone in corn flour utilizing novel self-enhanced electrochemiluminescence aptasensor based on NGQDs-NH_2-Ru@SiO_2 luminophore, Food Chem. 292 (2019) 98–105, https://doi.org/10.1016/j.foodchem.2019.04.050.

[24] L.P. Zong, X. Chen, D. Zhu, X.J. Li, F. Li, S. Cosnier, X.J. Zhang, R.S. Marks, D. Shan, Schiff base complexes with covalently anchored luminophores: self-enhanced electrochemiluminescence detection of neomycin, ACS Sens. 7 (10) (2022) 3085–3093, https://doi.org/10.1021/acssensors.2c01425.

[25] C. Wang, N. Zhang, D. Wei, R. Feng, D. Fan, L. Hu, Q. Wei, H. Ju, Double electrochemiluminescence quenching effects of Fe_3O_4@PDA-Cu_XO towards self-enhanced $Ru(bpy)_3^{2+}$ functionalized MOFs with hollow structure and it application to procalcitonin immunosensing, Biosens. Bioelectron. 142 (2019), 111521, https://doi.org/10.1016/j.bios.2019.111521.

[26] J. Fang, J. Li, R. Feng, L. Yang, L. Zhao, N. Zhang, G. Zhao, Q. Yue, Q. Wei, W. Cao, Dual-quenching electrochemiluminescence system based on novel acceptor CoOOH@Au NPs for early detection of procalcitonin, Sens. Actuators, B 332 (2021), 129544, https://doi.org/10.1016/j.snb.2021.129544.

[27] M.Y. Wang, W.J. Jing, L.J. Wang, L.P. Jia, R.N. Ma, W. Zhang, L. Shang, X.J. Li, Q. W. Xue, H.S. Wang, Electrochemiluminescence detection of miRNA-21 based on dual signal amplification strategies: duplex-specific nuclease -mediated target recycle and nicking endonuclease-driven 3D DNA nanomachine, Biosens. Bioelectron. 226 (2023), 115116, https://doi.org/10.1016/j.bios.2023.115116.

[28] W. Liang, Y. Zhuo, C. Xiong, Y. Zheng, Y. Chai, R. Yuan, A sensitive immunosensor via in situ enzymatically generating efficient quencher for electrochemiluminescence of iridium complexes doped SiO_2 nanoparticles, Biosens. Bioelectron. 94 (2017) 568–574, https://doi.org/10.1016/j.bios.2017.03.056.

[29] X. Huang, X. Huang, A. Zhang, B. Zhuo, F. Lu, Y. Chen, W. Gao, Quenching of the electrochemiluminescence of Ru-complex tagged shared-stem hairpin probes by graphene oxide and its application to quantitative turn-on detection of DNA, Biosens. Bioelectron. 70 (2015) 441–446, https://doi.org/10.1016/j.bios.2015.03.072.

[30] Q. Yue, X. Li, J. Fang, M. Li, J. Zhang, G. Zhao, W. Cao, Q. Wei, Oxygen free radical scavenger PtPd@PDA as a dual-mode quencher of electrochemiluminescence immunosensor for the detection of AFB1, Anal. Chem. 94 (33) (2022) 11476–11482, https://doi.org/10.1021/acs.analchem.2c00788.

[31] M.L. Alfieri, T. Weil, D.Y.W. Ng, V. Ball, Polydopamine at biological interfaces, Adv. Colloid Interface Sci. 305 (2022), 102689, https://doi.org/10.1016/j.cis.2022.102689.

[32] K. Cui, B. Yan, Y. Xie, H. Qian, X. Wang, Q. Huang, Y. He, S. Jin, H. Zeng, Regenerable urchin-like Fe_3O_4@PDA-Ag hollow microspheres as catalyst and adsorbent for enhanced removal of organic dyes, J. Hazard Mater. 350 (2018) 66–75, https://doi.org/10.1016/j.jhazmat.2018.02.011.

[33] L. Luo, X. Liu, X. Bi, L. Li, T. You, Dual-quenching effects of methylene blue on the luminophore and co-reactant: application for electrochemiluminescent-electrochemical ratiometric zearalenone detection, Biosens. Bioelectron. 222 (2023), 114991, https://doi.org/10.1016/j.bios.2022.114991.

[34] J. Liu, Y. Chen, W. Wang, J. Feng, M. Liang, S. Ma, X. Chen, "Switch-On" fluorescent sensing of ascorbic acid in food samples based on carbon quantum dots-MnO_2 probe, J. Agric. Food Chem. 64 (1) (2016) 371–380, https://doi.org/10.1021/acs.jafc.5b05726.

[35] L. Cao, Z. Lin, F. Peng, et al., Self-supporting metal-organic layers as single-site solid catalysts, Angew. Chem., Int. Ed. 55 (16) (2016) 4962–4966.

[36] Y. Zhang, Z. Lyu, Z. Chen, S. Zhu, Y. Shi, R. Chen, M. Xie, Y. Yao, M. Chi, M. Shao, Y. Xia, Maximizing the catalytic performance of Pd@Au_xPd_{1-x} nanocubes in H_2O_2 production by reducing shell thickness to increase compositional stability, Angew. Chem., Int. Ed. 60 (36) (2021) 19643–19647, https://doi.org/10.1002/anie.202105137.

[37] S. Shi, X. Han, J. Liu, X. Lan, J. Feng, Y. Li, W. Zhang, J. Wang, Photothermal-boosted effect of binary CuFe bimetallic magnetic MOF heterojunction for high-

performance photo-Fenton degradation of organic pollutants, Sci. Total Environ. 795 (2021), 148883, https://doi.org/10.1016/j.scitotenv.2021.148883.
[38] J. Chen, J. Zhao, J. Feng, D. Wu, H. Ma, X. Ren, Q. Wei, H. Ju, Photoelectrochemical immunosensor based on a 1D Fe_2O_3/3D Cd-$ZnIn_{2.2}S_y$ heterostructure as a sensing platform for ultrasensitive detection of neuron-specific enolase, Anal. Chem. 94 (50) (2022) 17396–17404, https://doi.org/10.1021/acs.analchem.2c02645.
[39] X. Wei, M.J. Zhu, Z. Cheng, M. Lee, H. Yan, C. Lu, J.J. Xu, Aggregation-Induced electrochemiluminescence of carboranyl carbazoles in aqueous media, Angew. Chem., Int. Ed. 58 (10) (2019) 3162–3166, https://doi.org/10.1002/anie.201900283.
[40] H. Wang, L. Peng, Y. Chai, R. Yuan, High-sensitive electrochemiluminescence C-peptide biosensor via the double quenching of dopamine to the novel Ru(II)-Organic complex with dual intramolecular self-catalysis, Anal. Chem. 89 (20) (2017) 11076–11082, https://doi.org/10.1021/acs.analchem.7b03125.
[41] C. Zhao, Z. Xie, C. Ma, X. Deng, C. Hong, S. Sun, Highly stable hybrid ligand Double-Enhanced electrochemiluminescence for sensitive detection of Cu^{2+}, Microchem. J. 185 (2023), 108237 https://doi.org/10.1016/j.microc.2022.108237.
[42] X. Yue, Z. Zhu, M. Zhang, Z. Ye, Reaction-based turn-on electrochemiluminescent sensor with a ruthenium(II) complex for selective detection of extracellular hydrogen sulfide in rat brain, Anal. Chem. 87 (3) (2015) 1839–1845, https://doi.org/10.1021/ac503875j.
[43] Y. Chu, T. Han, A. Deng, L. Li, J.J. Zhu, Resonance energy transfer in electrochemiluminescent and photoelectrochemical bioanalysis, TrAC Trends in Anal. Chem. 123 (2020), 115745, https://doi.org/10.1016/j.trac.2019.115745.
[44] F. Zu, F. Yan, Z. Bai, J. Xu, Y. Wang, Y. Huang, X. Zhou, The quenching of the fluorescence of carbon dots: a review on mechanisms and applications, Microchim. Acta 184 (7) (2017) 1899–1914, https://doi.org/10.1007/s00604-017-2318-9.
[45] A. Devadoss, C. Dickinson, T.E. Keyes, R.J. Forster, Electrochemiluminescent Metallopolymer−Nanoparticle composites: nanoparticle size effects, Anal. Chem. 83 (6) (2011) 2383–2387, https://doi.org/10.1021/ac102697c.
[46] W.X. Lv, Q.T. Yang, Q. Li, H.Y. Li, F. Li, Quaternary ammonium salt-functionalized tetraphenylethene derivative boosts electrochemiluminescence for highly sensitive aqueous-phase biosensing, Anal. Chem. 92 (2020) 11747–11754.
[47] J.F. Chang, L. Yu, T. Hou, R.X. Hu, F. Li, Direct and specific detection of glyphosate using a phosphatase-like nanozyme-mediated chemiluminescence strategy, Anal. Chem. 95 (2023) 4479–4485.
[48] X. Zhang, J. Xu, J. Zhong, L. Zhong, Z. Mai, D. Sun, H. Zhai, A novel fluorescence sensor for sensitive detection of zearalenone using a polyvinylpyrrolidone-modified Zr(IV)-based metal-organic framework, Sens. Actuators, B 395 (2023), https://doi.org/10.1016/j.snb.2023.134516.
[49] L. Wang, H. Li, Y. Yang, D. Zhang, M. Wu, B. Pan, B. Xing, Identifying structural characteristics of humic acid to static and dynamic fluorescence quenching of phenanthrene, 9-phenanthrol, and naphthalene, Water Res. 122 (2017) 337–344, https://doi.org/10.1016/j.watres.2017.06.010.
[50] H. Liang, Y. Luo, Y. Li, Y. Song, L. Wang, An immunosensor using electroactive COF as signal probe for electrochemical detection of carcinoembryonic antigen, Anal. Chem. 94 (13) (2022) 5352–5358, https://doi.org/10.1021/acs.analchem.1c05426.
[51] H. Yang, Y. Xu, Q. Hou, Q. Xu, C. Ding, Magnetic antifouling material based ratiometric electrochemical biosensor for the accurate detection of CEA in clinical serum, Biosens. Bioelectron. 208 (2022), 114216, https://doi.org/10.1016/j.bios.2022.114216.
[52] L. Lu, X. Hu, R. Zeng, Q. Lin, X. Huang, Q. Wei, D. Tang, D. Knopp, Ag/MoO_3-Pd-mediated gasochromic reaction: an efficient dual-mode photoelectrochemical and photothermal immunoassay, Biosens. Bioelectron. 230 (2023), 115267, https://doi.org/10.1016/j.bios.2023.115267.
[53] Z. Song, Y. Suo, S. Duan, S. Zhang, L. Liu, B. Chen, Z. Cheng, NIR-II fluorescent nanoprobe-labeled lateral flow biosensing platform: a high-performance point-of-care testing for carcinoembryonic antigen, Biosens. Bioelectron. 224 (2023), 115063, https://doi.org/10.1016/j.bios.2023.115063.
[54] Y. Su, W. Lai, Y. Liang, C. Zhang, Novel cloth-based closed bipolar solid-state electrochemiluminescence (CBP-SS-ECL) aptasensor for detecting carcinoembryonic antigen, Anal. Chim. Acta 1206 (2022), 339789, https://doi.org/10.1016/j.aca.2022.339789.
[55] W. Zhang, L. Chen, K. Yang, L. Wang, B. Han, S. Sun, J. Wen, An electrochemiluminescence immunosensor based on functionalized metal organic layers as emitters for sensitive detection of carcinoembryonic antigen, Sens. Actuators, B 393 (2023), https://doi.org/10.1016/j.snb.2023.134317.
[56] D. Zhang, M. Gao, X. Xue, X. Ren, R. Feng, D. Wu, X. Liu, Q. Wei, Triple signal-enhanced electrochemiluminescence strategy using iron-based metal-organic frameworks modified with Ru(II) complexes for carcino-embryonic antigen detection, Talanta 267 (2024) 125239. https://doi.org/10.1016/j.talanta.2023.125239..
[57] J.T. Cao, Y.X. Dong, Y. Ma, B. Wang, S.H. Ma, Y.M. Liu, A ternary CdS@Au-g-C_3N_4 heterojunction-based photoelectrochemical immunosensor for prostate specific antigen detection using graphene oxide-CuS as tags for signal amplification, Anal. Chim. Acta 1106 (2020) 183–190.
[58] H.-J. Xiao, Y.-L. Wang, C.-J. Liu, Z.-H. Gao, S.-W. Ren, J.-T. Cao, Y.-M. Liu, Liposome-Mediated in situ formation of Ag_3PO_4/AgBr/Br-CN ternary nanostructures on photoanodes for photoelectrochemical immunoassay, ACS Appl. Nano Mater. 6 (2023) 6496–6503.
[59] J.T. Cao, J.L. Lv, X.J. Liao, S.H. Ma, Y.M. Liu, A membraneless self-powered photoelectrochemical biosensor based on Bi_2S_3/$BiPO_4$ heterojunction photoanode coupling with redox cycling signal amplification strategy, Biosens. Bioelectron. 195 (2022), 113651.
[60] J. Chen, J. Zhao, R. Feng, H. Ma, H. Wang, X. Ren, Q. Wei, H. Ju, Competitive photoelectrochemical aptamer sensor based on a Z-scheme Fe2O3/g-C3N4 heterojunction for sensitive detection of lead ions, J. Hazard Mater. 459 (2023), 132122, https://doi.org/10.1016/j.jhazmat.2023.132122.
[61] J. Chen, N. Song, N. Zhang, Z. Gao, D. Wu, H. M, X. Ren, Q. Wei, Smartphone-controlled portable photoelectrochemical immunosensor for point-of-care testing of carcinoembryonic antigen, Chem. Eng. J. 473 (2023), 145276, https://doi.org/10.1016/j.cej.2023.145276.
[62] Z. Xie, M. Shao, Z. Liu, X. Ren, M. Gao, H. Ma, N. Zhang, Q. Wei, Ultrasensitive aggregation-induced electrochemiluminescence sensor for dopamine detection in polymer hydrogel system, Sens. Actuators, B 398 (2024) 134781. https://doi.org/10.1016/j.snb.2023.134781..